Volume 10
Number 10
October 2023
Pages 3857–4636

Materials Horizons

rsc.li/materials-horizons

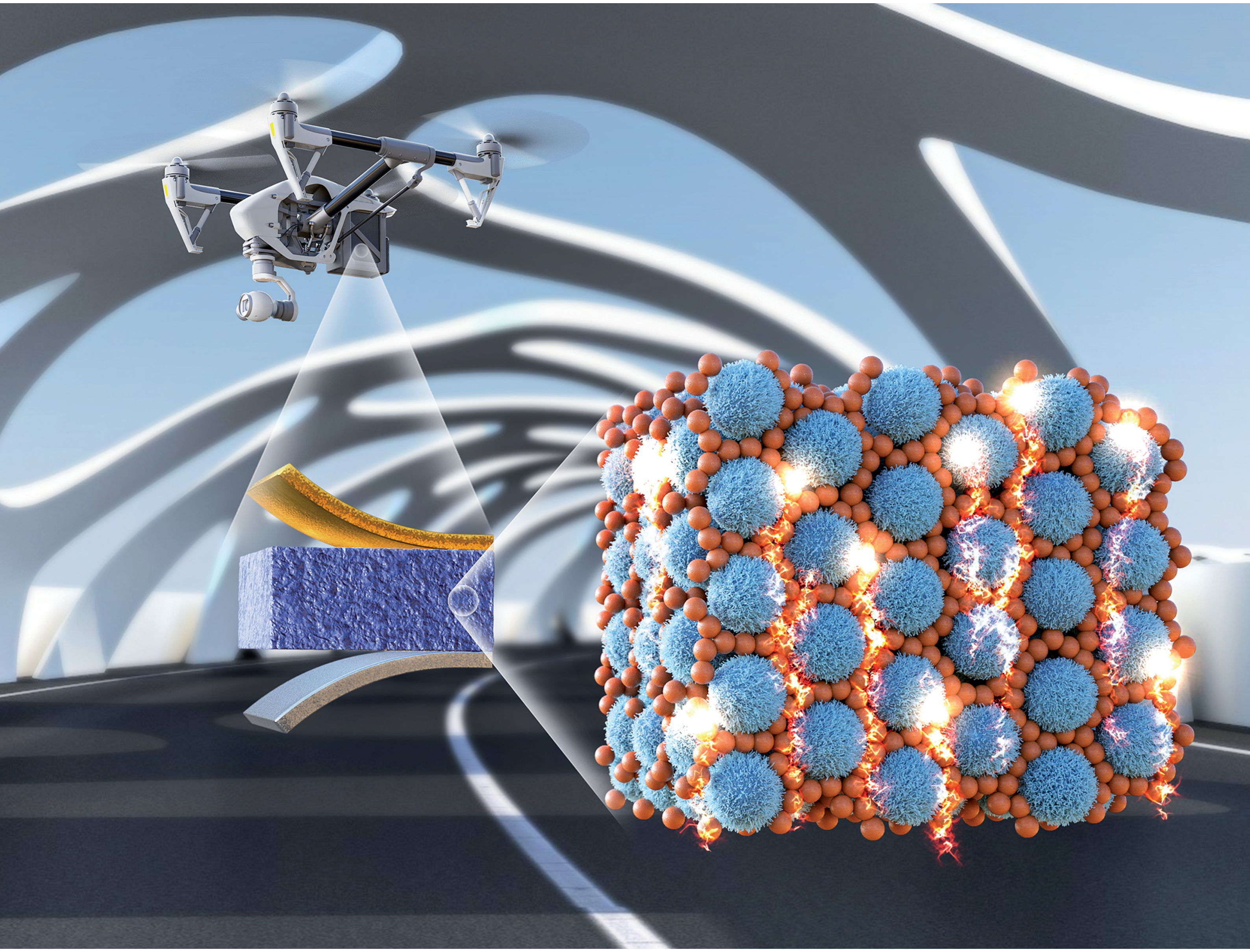

ISSN 2051-6347

ROYAL SOCIETY
OF **CHEMISTRY**

COMMUNICATION
Boram Kim and Moon Jeong Park
All-solid-state lithium–sulfur batteries enabled by single-ion conducting binary nanoparticle electrolytes

Materials
Horizons

ROYAL SOCIETY
OF CHEMISTRY

COMMUNICATION

View Article Online
View Journal | View Issue

Check for updates

Cite this: *Mater. Horiz.*, 2023, **10**, 4139

Received 14th June 2023,
Accepted 1st August 2023

DOI: 10.1039/d3mh00913k

rsc.li/materials-horizons

All-solid-state lithium–sulfur batteries enabled by single-ion conducting binary nanoparticle electrolytes†

Boram Kim and Moon Jeong Park *

We designed solid-state hybrid electrolytes with single-ion conducting properties by co-assembling binary core–shell polymer nanoparticles. By controlling the nanoparticle size and number, we created superlattices that optimized the Li^+ concentration and transport. The electrolytes exhibited a remarkable ionic conductivity (10^{-4} S cm^{-1}), lithium transference number (0.94), electrochemical stability (up to 6 V), and modulus (0.12 GPa) at 25 °C. The mechanical strength of these electrolytes depended minimally on temperature at 25–150 °C because of the robustness of the cores. When implemented in Li–S batteries with no liquids, they demonstrated an initial discharge capacity of 1090 mA h g^{-1} at 0.05C, a cycle life of over 200 cycles, and a rate capability with a discharge capacity of 627 mA h g^{-1} at 3C.

Moon Jeong Park

Sincere congratulations on the 10th anniversary of Materials Horizons! As the flagship journal of the RSC in the realm of materials science, it has unfailingly cultivated a distinguished reputation for excellence. Serving on the advisory board since 2020 is a profound honor and privilege. We are thrilled to contribute our article on the ingenious design of all-solid-state lithium-sulfur batteries, holding promise for enhanced performance and safety in future energy storage systems. With immense enthusiasm and commitment, we eagerly await the opportunity to further enrich the pages of this outstanding journal with our future contributions. Best wishes to Materials Horizons!.

New concepts

The pressing need for safer alternatives to liquid electrolytes in lithium-ion batteries led to remarkable progress in all-solid-state lithium batteries. This work presents an ingenious design of solid-state single-ion electrolytes using superlattices of two types of core–shell nanoparticles. These electrolytes demonstrate an ionic conductivity of 10^{-4} S cm^{-1}, a lithium transference number of 0.94, exceptional electrochemical stability up to 6 V, and elastic moduli of 0.12 GPa at 25 °C. Furthermore, they maintain mechanical resilience across a temperature range of 25 to 150 °C, addressing the longstanding trade-off between ionic conductivity and mechanical strength. When integrated into lithium-sulfur batteries without any liquid components, a rarity in the literature, they demonstrate excellent specific capacity, coulombic efficiency, cycle life, and rate performance.

Introduction

The demand for safer alternatives to liquid electrolytes in lithium-ion batteries has stimulated the development of all-solid-state lithium batteries.[1–3] These advanced batteries aim to mitigate potential hazards associated with flammability and dendrite formation during operation.[4–6] Additionally, the integration of solid-state electrolytes creates opportunities to improve the energy and power densities of lithium batteries by enabling the direct utilization of lithium metal as the anode.[7]

Inorganic solid electrolytes have emerged as highly promising materials to advance battery technology owing to their advantageous characteristics, including high ionic conductivity,[8] excellent thermal stability,[9] and the ability to operate at a high voltage.[10] Nevertheless, several obstacles have impeded the widespread adoption of inorganic electrolytes in lithium batteries, such as limited scalability in production,[10,11] poor interfacial interactions with electrodes,[12] and vulnerability to decomposition in ambient air.[13] To fully harness the potential of inorganic electrolytes in all-solid-state batteries, it is imperative to confront and overcome these challenges.

Extensive research has been devoted to developing advanced polymer electrolytes as promising alternatives to inorganic solid electrolytes.[14] The softness of polymers also enables the

---

Department of Chemistry, Division of Advanced Materials Science, Pohang University of Science and Technology (POSTECH), Pohang 37673, Korea. E-mail: moonpark@postech.ac.kr

† Electronic supplementary information (ESI) available. See DOI: **https://doi.org/10.1039/d3mh00913k**

design of flexible batteries that satisfy the demands of next-generation wearable devices.[3,15] However, despite being the focus of extensive research for several decades, these materials have encountered significant obstacles that collectively hinder their viability in practical applications. These challenges include the trade-off between ionic conductivity and mechanical strength,[16,17] difficulties in operating at low temperatures owing to polymer crystallization,[7] loss of mechanical strength at elevated temperatures,[18] limited electrochemical stability below 5 V,[19] and insufficient rate performance.[15]

Researchers are actively exploring innovative polymer designs to address these limitations. These endeavors encompass diverse strategies to facilitate rapid ion/polymer relaxation and improve dielectric properties,[16,19,20] including the precise manipulation of polymer chain structures,[21,22] end groups,[17,23] and local ion concentrations.[24] In pursuit of these goals, an alternative approach has arisen in the form of composite electrolytes that harness the synergistic properties of polymers and ceramic fillers. Silica (SiO_2), alumina (Al_2O_3), and titania (TiO_2) are the most commonly employed ceramic fillers,[4,25] offering tunable particle sizes, dimensions, and surface functionalities.[26–28]

However, these composite electrolytes often exhibit poor homogeneity at high filler concentrations, necessitating the modification of the filler surfaces with polymeric shells to achieve uniform dispersion.[29,30] For instance, researchers have covalently grafted polyethylene oxide (PEO) chains[31] or polymerized ionic liquids[32,33] onto ceramic fillers, and the ionic conductivity of such electrolytes could be optimized by controlling the density and length of the grafting chains.[34] This approach has also been extended to single-ion polymer electrolytes utilizing active fillers such as perovskites, garnet, LISICON, and sulfides.[35] These efforts primarily aimed to address dendrite formation and poor electrochemical stability when combined with high-voltage cathodes in batteries using salt-doped PEO-based electrolytes with low lithium transference numbers (t_{Li^+}, <0.3).[36] Nonetheless, the challenge of achieving a uniform distribution of discrete particles hinders the creation of interconnected ionic pathways, limiting the attainment of ionic conductivity comparable to that of salt-doped polymer electrolytes without compromising the mechanical strength.

In this study, we developed solid-state single-ion conducting hybrid electrolytes using binary core–shell nanoparticles (NPs) with large surface areas and excellent thermodynamic compatibility. By controlling the size and number ratio of the NPs, we successfully co-assembled superlattices that facilitated efficient Li^+ conduction *via* highly interconnected pathways. The binary polymer NPs (BNPs) electrolytes exhibited a t_{Li^+} of 0.94, ionic conductivity of 10^{-4} S cm^{-1}, and an elastic modulus of 0.12 GPa at 25 °C. Notably, the mechanical properties remained stable during temperature variations owing to the robust particle cores. We then tested all-solid-state Li–S batteries using BNPS electrolytes, which revealed high discharge capacities, excellent rate performance, and good cycling stability. Considering the scarcity of examples of all-solid-state Li–S batteries, our work represents a significant stride in advancing energy storage solutions.

Results and discussion

To achieve both single-ion conduction and mechanical stability over a wide temperature range in solid-state polymer electrolytes, we synthesized BNPs electrolytes. These electrolytes were developed by employing two distinct types of core–shell polymer NPs with mechanically robust cores and shells capable of facilitating Li^+ transport.

Fig. 1a illustrates the routes for synthesizing NPs with a crosslinked polystyrene (*x*-PS) core and a corona composed of poly(4-styrenesulfonyltrifluoromethylsulfonyl) imide, referred to hereafter as PS(LiTFSI) NPs. Specifically, NPs with an *x*-PS core and a poly(4-styrenesulfonate sodium) (PSS^-Na^+) corona were first prepared by the emulsion polymerization of styrene and divinyl benzene with an excess of styrene sulfonate sodium salt.[37] Subsequently, a two-step modification process was conducted to convert the $-SO_3^-Na^+$ groups into $-TFSI^-Li^+$ groups (Fig. S1, ESI†).

To enhance Li^+ transport within the BNPs electrolyte, as depicted in Fig. 1b, silica NPs with thiol surfaces were synthesized using a sol–gel reaction,[38] which were then used to synthesize PEO-grafted silica NPs (referred to as PEO NPs) *via* thiol-ene click chemistry, utilizing vinyl-terminated PEO with a molecular weight of 2 kg mol^{-1}. Thermogravimetric analysis (TGA) revealed that approximately 37 wt% PEO chains were grafted onto the silica NPs (Fig. S2, ESI†).

The size and shape of the PS(LiTFSI) NPs and PEO NPs were investigated using transmission electron microscopy (TEM), as shown in Fig. 1a and Fig. 1b, respectively. Bright-field TEM images revealed that the average diameters of the PS(LiTFSI) NPs and PEO NPs were 20 and 60 nm, respectively. Electron energy-loss spectroscopy corroborated the core–shell structures of the NPs. Based on the oxygen and carbon maps, the thickness of the PS(LiTFSI) shell was measured to be 3–4 nm, whereas that of the PEO shells was approximately 2–3 nm.

The co-assembled structures of the BNPs electrolyte formed according to the composition of the PEO NPs and PS(LiTFSI) NPs were investigated, with particular emphasis on BNPs electrolyte, in which PEO NPs constituted the major component. This stemmed from the fact that the PS(LiTFSI) chains exhibited a high glass transition temperature (T_g) exceeding 150 °C, which renders membrane fabrication impractical when PS(LiTFSI) NPs dominated the composition. By incorporating PS(LiTFSI) NPs as a minor component, smaller PS(LiTFSI) NPs were strategically located within the voids formed by the arrangement of larger PEO NPs.

Assuming uniform particle sizes, Fig. 2a schematically illustrates the envisaged co-assembled structures of BNPs with different compositions. Considering the densities of the components, a mass ratio of 6 : 1 between the PEO NPs and PS(LiTFSI) NPs corresponds to a number ratio of 1 : 3, leading to the formation of an AB_3 structure. Similarly, mass ratios of 3 : 1 and 3 : 2 between the PEO NPs and PS(LiTFSI) NPs were expected to yield AB_6 and AB_{12} structures, respectively.

To substantiate the proposed co-assembly of PEO NPs and PS(LiTFSI) NPs in the BNPs electrolyte, scanning electron

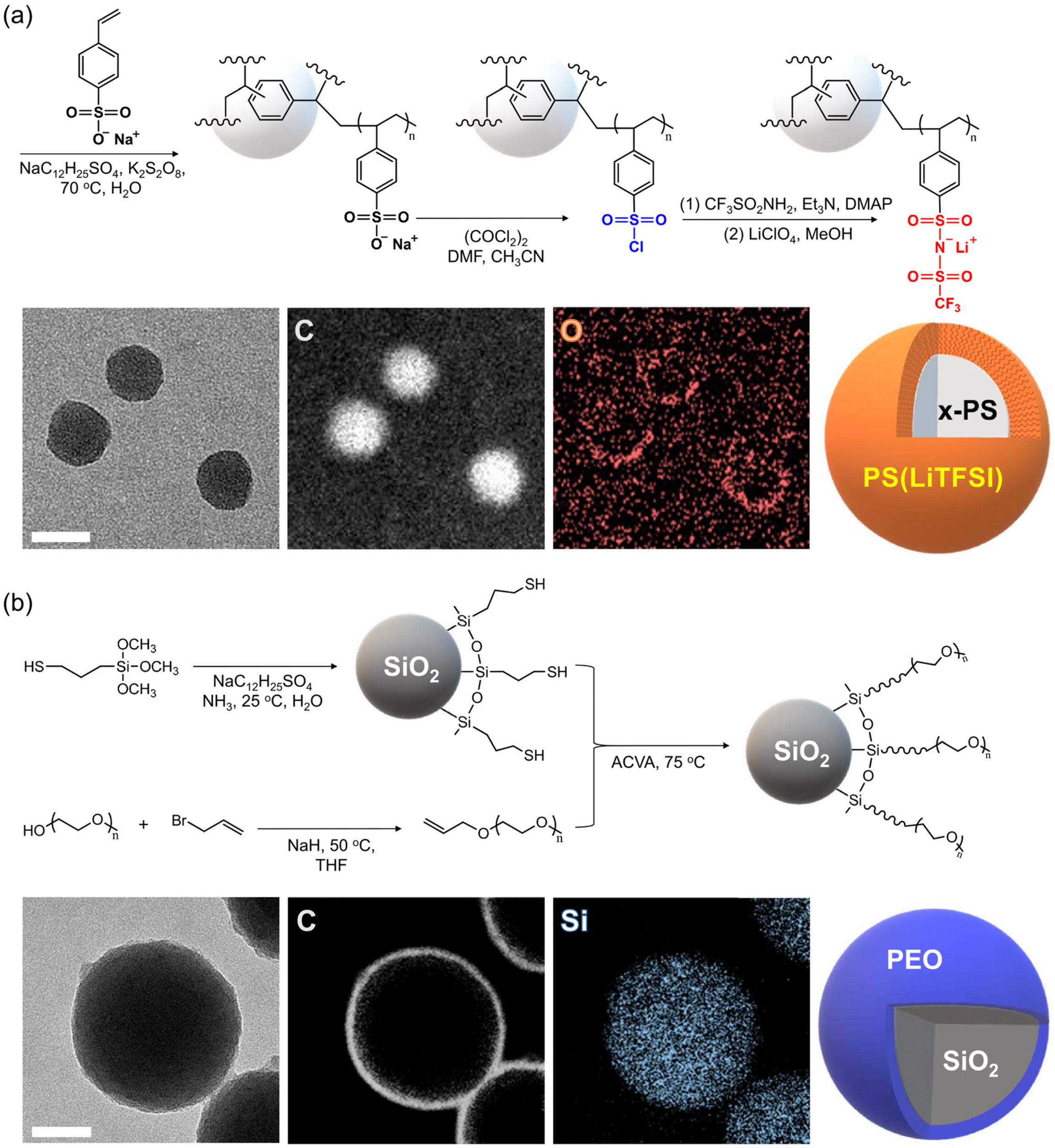

Fig. 1 Synthetic routes to two different types of core–shell polymer nanoparticles: (a) core-crosslinked PS(LiTFSI) nanoparticles and (b) PEO-grafted silica nanoparticles. Bright-field TEM images and elemental mappings of nanoparticles show the core–shell structures. C: carbon; O: oxygen; Si: silicon (scale bars: 20 nm).

microscopy (SEM) and TEM were performed. The resulting images in Fig. 2(b) provide compelling evidence that the surface of the PEO NPs was uniformly covered by the PS(LiTFSI) NPs without any apparent macroscopic phase separation. Furthermore, increasing the loading quantity of the PS(LiTFSI) NPs was confirmed to increase the degree of surface coverage.

TEM micrographs provide insightful visualizations of the different AB_n structures observed in the BNPs electrolyte achieved by manipulating the mass ratios between the PEO NPs and PS(LiTFSI) NPs. Fig. 2c highlights the distinct superlattice symmetries and variations in the spacing between the PEO NPs. Importantly, the interconnected structures of the PEO NPs remained intact for the AB_3 and AB_6 structures, which is crucial for minimizing dead ends in Li^+ transport. However, the arrangement of the PEO NPs was disrupted in the AB_{12}-structured BNPs, primarily because of the significant surface coverage of the PS(LiTFSI) NPs on the PEO NPs.

Next, we investigated the temperature-dependent ionic conductivity of the BNPs electrolyte with different co-assembled structures. To mitigate the issue of impeded ion transport caused by voids between the NPs, we introduced a solid-state additive (4 wt% dimethyl sulfone, DMS) or an ionic liquid (10 wt%, EMImTFSI) to fill these spaces using a blotting method after forming the superlattices. Due to the high

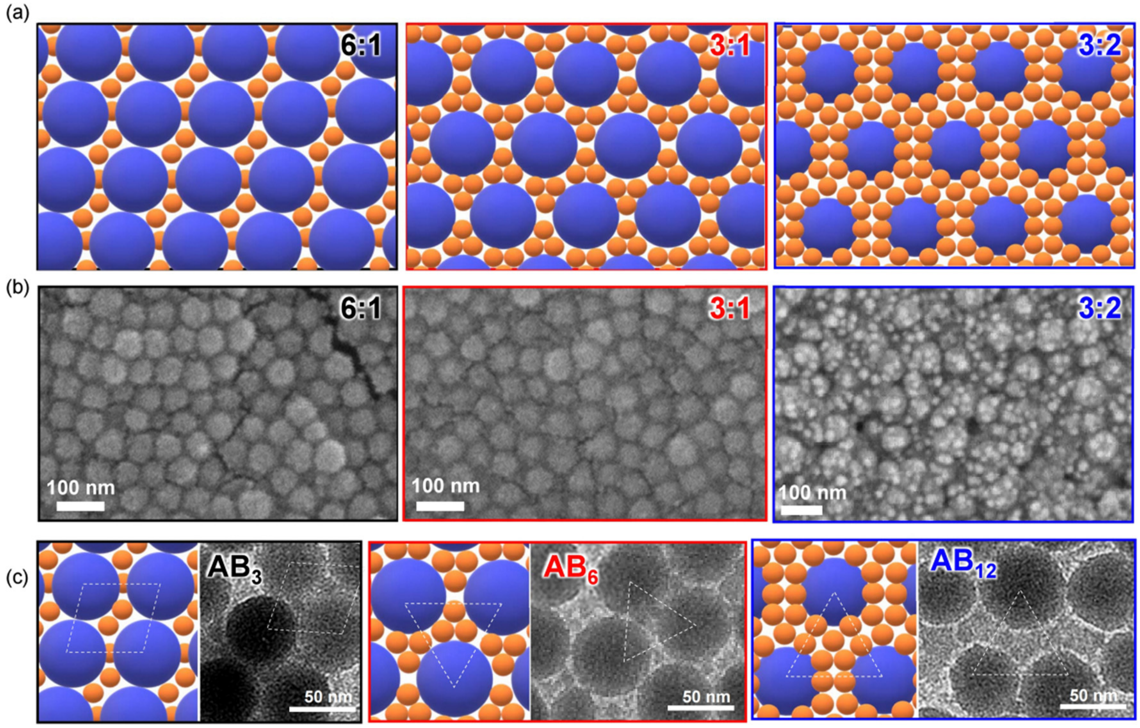

Fig. 2 (a) Schematic illustrations of self-assembled structures and (b) SEM images of BNPs electrolytes at various mass ratios of PEO NPs: PS(LiTFSI) NPs = 6 : 1, 3 : 1, and 3 : 2. (c) Schematics and bright field-TEM images of BNPs electrolytes with different mass ratios of PEO NPs: PS(LiTFSI) NPs = 6 : 1, 3 : 1, and 3 : 2, corresponding to AB_3, AB_6, and AB_{12} structures, respectively.

elasticity of the BNPs, the incorporation of these additives had minimal effect on the self-assembled morphology of the BNPs electrolyte. Representative X-ray scattering profiles in Fig. S3 (ESI†) provide a comparison of the BNPs with and without DMS, indicating negligible changes in the spacing between PEO NPs within the BNPs upon the addition of DMS. Additionally, we assessed the effect of NP co-assembly on the Li^+ transport rate by measuring the ionic conductivity of homopolymer blends of PEO and PS(LiTFSI) with the same molecular weight, type of additives, and composition.

As shown in Fig. 3a, the BNPs with the AB_6 structure (red filled symbols) exhibited the highest ionic conductivity, irrespective of the type of additive used. In contrast, BNPs with the AB_3 structure (black filled symbols) showed approximately 2–10 times lower conductivity than their AB_6 counterparts. This can be attributed to the decrease in the Li^+ concentration. Notably, neither the AB_3- nor AB_6-structured BNPs electrolyte exhibited a sharp decline in ionic conductivity with decreasing temperature, indicating PEO crystallinity was suppressed by physical confinement and effective interactions between the PEO NPs and PS(LiTFSI) NPs. The highest ionic conductivity observed for the BNPs electrolyte at room temperature was 0.6×10^{-4} S cm^{-1} when combined with EMImTFSI. This can be attributed to the enhanced local ion concentration and effective plasticizing effect provided by the liquid-state EMImTFSI. When incorporating the non-ionic solid-state DMS, the BNPs electrolytes exhibited the ionic conductivity of 0.3×10^{-5} S cm^{-1} at room temperature, which is still an order of magnitude higher than the conductivity of neat BNPs (Fig. S4, ESI†). This highlights the advantageous effect of incorporating DMS in BNPs, as it facilitates the dissociation of Li^+ ions from PS(LiTFSI) NPs upon contact with DMS localized in voids, facilitated by the high dielectric constant of DMS. Surprisingly, despite having twice the Li^+ concentration with respect to that of the AB_6 structure, the BNPs with the AB_{12} structure (blue filled symbols) exhibited significantly lower in conductivity. This finding can be rationalized by the high T_g value of the PS(LiTFSI) chains coupled with the reduced connectivity of the PEO NPs.

The conductivity behavior of these BNPs electrolyte deviated remarkably from that of the PEO/PS(LiTFSI) blend electrolytes. As depicted by the open symbols in Fig. 3a, when employing a PEO/PS(LiTFSI) mass ratio of 3 : 2, a slightly higher ionic conductivity was observed, but overall, the conductivity did not substantially depend on the composition. The conductivity of blend samples remained nearly unaffected with or without DMS (Fig. S4, ESI†), indicating that the non-ionic DMS does not directly contribute to ion transport. Importantly, in contrast to that of the BNPs electrolyte, the ionic conductivity of the blended electrolytes significantly decreased when the sample temperature decreased below the melting temperature of PEO, as indicated by the red shaded region. Consequently, regardless of the blend composition, the conductivity at room temperature remained on the order of 10^{-6} S cm^{-1} or became unmeasurable. This behavior was consistently observed in all blend samples. The conductivity results were consistent with those obtained from differential scanning calorimetry (Fig. S5, ESI†)

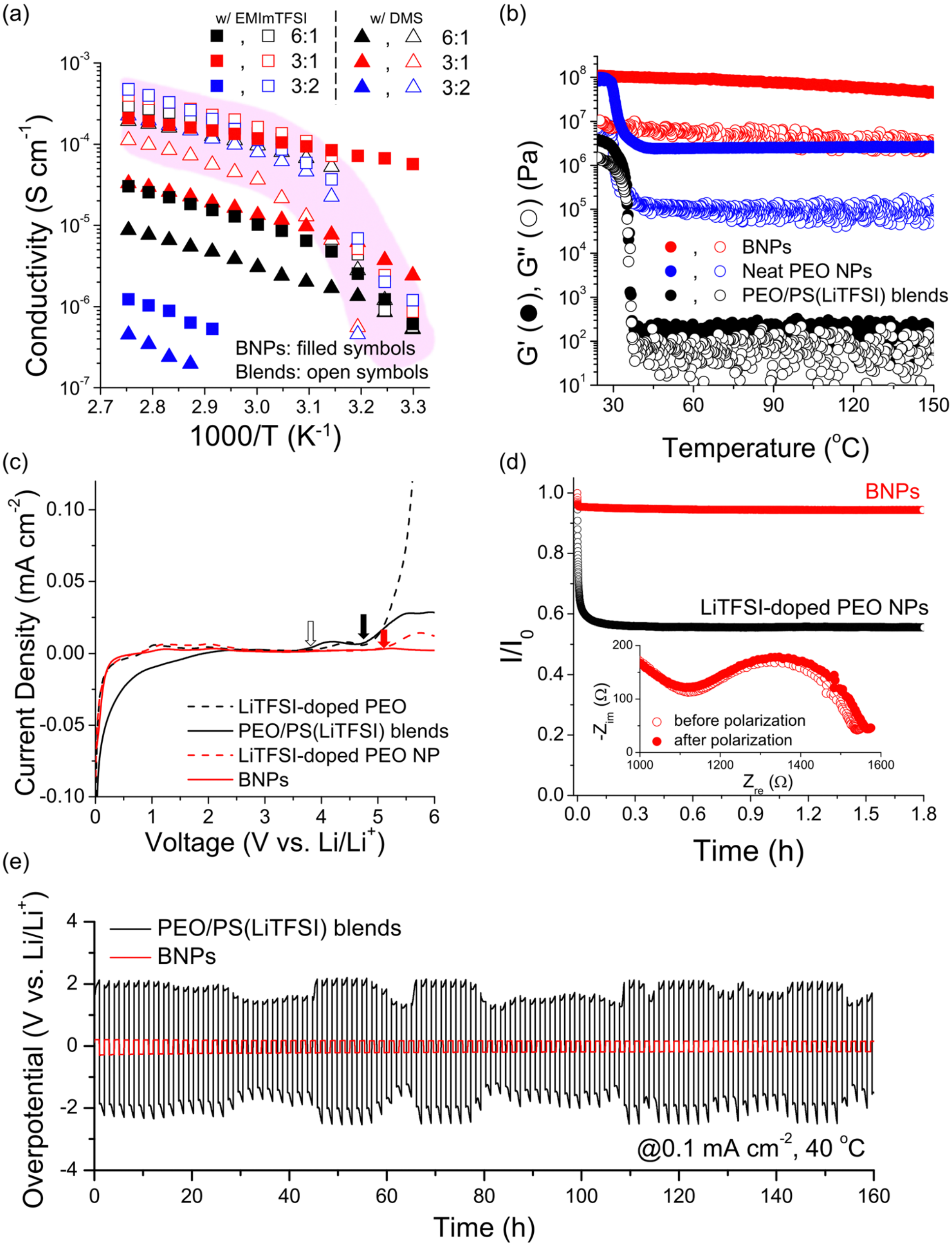

Fig. 3 (a) Ionic conductivities of BNPs electrolytes with EMImTFSI (filled squares) and DMS (filled triangles) as a functional of temperature, compared to PEO/PS(LiTFSI) blend electrolytes (open symbols). (b) Storage and loss moduli of the AB_6-structured BNPs with DMS, compared to PEO/PS(LiTFSI) blends with the same composition and additive, measured at strain of 0.1%, frequency of 0.5 rad s^{-1}, and scan rate of 1 °C min^{-1}. Moduli of neat PEO NPs are also shown for a comparison. (c) Linear sweep voltammograms of BNPs with DMS, compared to other type of dual- and single-ion polymer electrolytes measured at 1 mV s^{-1} and 40 °C. Inverted arrows indicate the onset of oxidative decomposition. (d) Polarization tests for Li symmetric cells using BNPs and LiTFSI-doped PEO NPs at ΔV = 50 mV and 40 °C. Nyquist plots of the Li/BNPs/Li cells obtained before and after the polarization are shown in the inset. (e) Galvanostatic Li plating/stripping tests of BNPs and PEO/PS(LiTFSI) blends at J = 0.1 mA cm^{-2} and 40 °C.

and X-ray powder diffraction (Fig. S6, ESI†), underscoring the pivotal role of the NP geometry in enabling the operation of all-solid-state lithium batteries at room temperature.

The BNPs electrolyte with a co-assembled structure of PEO NPs and PS(LiTFSI) NPs exhibited significant advantages over PEO/PS (LiTFSI) blend electrolytes in enhancing the mechanical properties. Fig. 3b shows the representative storage (G') and loss (G'') moduli of the AB_6-structured BNPs with DMS. Note that our focus shifted toward incorporating DMS as a solid-state additive, as certain electrolytes containing EMImTFSI have displayed rapid water sorption upon exposure to the ambient atmosphere, which was attributed to the hygroscopic properties of EMImTFSI. At 23 °C, an elastic modulus of 0.12 GPa and a tan δ of 0.076 were attained, with minimal variation in values across the temperature range of 23–150 °C. This stability is ascribed to the tightly packed PEO NPs and PS(LiTFSI) NPs, which possess mechanically robust cores. The strong interactions between the PEO chains and the PS(LiTFSI) chains impeded the viscous movement of the PEO NPs. In contrast, the elastic modulus of PEO/PS(LiTFSI) blends were 43 MPa at 23 °C but rapidly decreased during the melting transition of PEO. At 40 °C, the PEO/PS(LiTFSI) blends became liquid, with a significantly reduced G' value of only 0.22 kPa.

Notably, because of the silica cores in PEO NPs, neat PEO NPs exhibited an elastic modulus of 90 MPa at 23 °C. However, the PEO melting transition is associated with an abrupt drop in both G' and G'' by more than an order of magnitude, resulting in a low modulus of 4.2 MPa above 40 °C. These results unequivocally establish the remarkable superiority of the BNPs electrolyte, which avoid the conventional trade-off between conductivity and mechanical strength through the unique design of superlattice structures, thereby representing a significant breakthrough in the field of solid-state single-ion electrolytes.

Fig. S7 (ESI†) displays a comparison plot of conductivity–modulus relationship for BNPs electrolytes and the solid-state single-ion polymer electrolytes reported in the literature. Quasi-solid electrolytes containing additional salts or liquid additives were not taken into consideration. The results demonstrate the superior performance of BNPs in comparison to all previously reported single-ion polymer electrolytes. Of particular significance is the minimal decrease in modulus despite the substantial increase in conductivity.

Fig. 3c demonstrates the distinctly higher electrochemical stability of the BNPs electrolyte compared to that of other dual- or single-ion polymer electrolytes. In contrast to the limited electrochemical stability observed in LiTFSI-doped PEO homopolymers and PEO/PS(LiTFSI), wherein the TFSI^- anions and EO backbones evidently decomposed (indicated by open black and filled black arrows, respectively), the BNPs and LiTFSI-doped PEO NPs demonstrated a wider electrochemical stability window surpassing 5.2 V (indicated by the filled red arrow). This superior stability can be attributed to the covalently tethered TFSI^- anions and the densely packed PEO chains grafted onto the silica cores, which effectively shielded the lone-pair electrons of the EO units.[2] In particular, the BNPs electrolyte exhibited exceptional oxidative stability, displaying no signs of oxidative decomposition of PEO even at 6 V. These results corroborate the efficient interactions between the PEO NPs and PS(LiTFSI) NPs in the BNPs electrolyte, facilitated by the large surface area of the PS(LiTFSI) NPs. These findings underscore the significant potential of BNPs electrolyte as high-voltage cathode materials.

Note that at a temperature of 25 °C, all control electrolytes, including PEO/PS(LiTFSI) blends, LiTFSI-doped PEO NPs, and LiTFSI-doped PEO, exhibited poor interfacial contact with the electrodes because of PEO crystallization, in contrast with the BNPs electrolyte. As a result, the temperature had to be raised to 40 °C to test the control samples.

Polarization experiments were carried out using Li symmetric cells combined with electrochemical impedance spectroscopy to evaluate the t_{Li^+} values of the BNPs electrolyte. Fig. 3d compares the normalized current densities measured over for 2 h after subjecting the cells to polarization at 50 mV and 40 °C. The Li/BNPs/Li cell exhibited an initial current density of 26.9 μA cm^{-2}, which remained steady at 25.4 μA cm^{-2} throughout the measurement. By analyzing the interfacial resistance values before and after polarization (as depicted in the inset of the Nyquist plots), the Bruce–Vincent method[39] determined a t_{Li^+} value of 0.94, thereby confirming the single-ion conducting properties of the BNPs electrolyte. In contrast, the LiTFSI-doped PEO NPs exhibited a significant reduction in current density, resulting in a low t_{Li^+} value of 0.23, which is consistent with the values for Li-salt-doped PEO-based electrolytes reported in the literature.[36]

The utilization of BNPs in Li cells also resulted in a uniform lithium morphology, thus improving cycling stability during lithium stripping and plating. This improvement is clearly shown in Fig. 3e, wherein the overpotential of the cell containing BNPs remains consistently low during lithium stripping and plating at a constant current density of 0.1 mA cm^{-2} and 40 °C. In contrast, the cells with the PEO/PS(LiTFSI) blends displayed significantly higher and unstable overpotential values, which was attributed to their unstable interface between Li metal and electrolytes. These findings confirm that the enhanced cycling stability provided by the BNPs primarily arises from the mechanically robust cores, the evident nano-confinement, and the prevention of anion depletion through high t_{Li^+} values. As a result, dendrite formation and subsequent short-circuiting were successfully prevented for over 160 h, in agreement with the model proposed by Chazalviel *et al.*[40]

We also investigated the battery performance of AB_6-structured BNPs utilizing sulfur cathodes to develop nonflammable, nonexplosive, high-energy-density all-solid-state lithium batteries. To construct the sulfur cathode, we conducted the inverse vulcanization of elemental sulfur using tetramino-benzoquinone (TABQ) to synthesize sulfur-rich polymers (sulfur content of 90 wt%), which is referred to as poly(S-TABQ).[41] The sulfur cathode was then fabricated doctor blading technique using poly(S-TABQ) as the active material and aluminum as the current collector.

Fig. 4a shows the representative voltage profiles during the galvanostatic discharge and charge processes of Li–S cells using BNPs electrolyte with DMS at 0.05C and 25 °C. The initial discharge and charge capacities were 1090 and 1147 mA h g^{-1}, respectively, resulting in a coulombic efficiency (CE) of 95%. The CE values quickly reached a high value (> 99%) within the first five cycles, accompanied by a discharge capacity of 1008 mA h g^{-1}. Notably, the Li/BNPs/poly(S-TABQ) cell demonstrated a small polarization of 0.17 V, indicating efficient charge-transfer kinetics across the single-ion-conducting BNPs electrolyte.

It is worth highlighting that the Li/BNPs/poly(S-TABQ) cell exhibited two distinct plateaus at 25 °C, indicating a "solid-liquid-solid" transition with multi-step polysulfide reactions. This can be attributed to the significant reduction in the crystallinity of the PEO NPs within the solid-state BNPs, resulting from their interactions with PS(LiTFSI) chains and confinement, which led to the molten state of the PEO shells.

The discharge capacity after 50 cycles was 873 mA h g^{-1}, as plotted in Fig. 4b, corresponding to a capacity retention of 87%, while maintaining a high CE value (> 99%) throughout extended cycling. These results suggest the formation of a stable solid

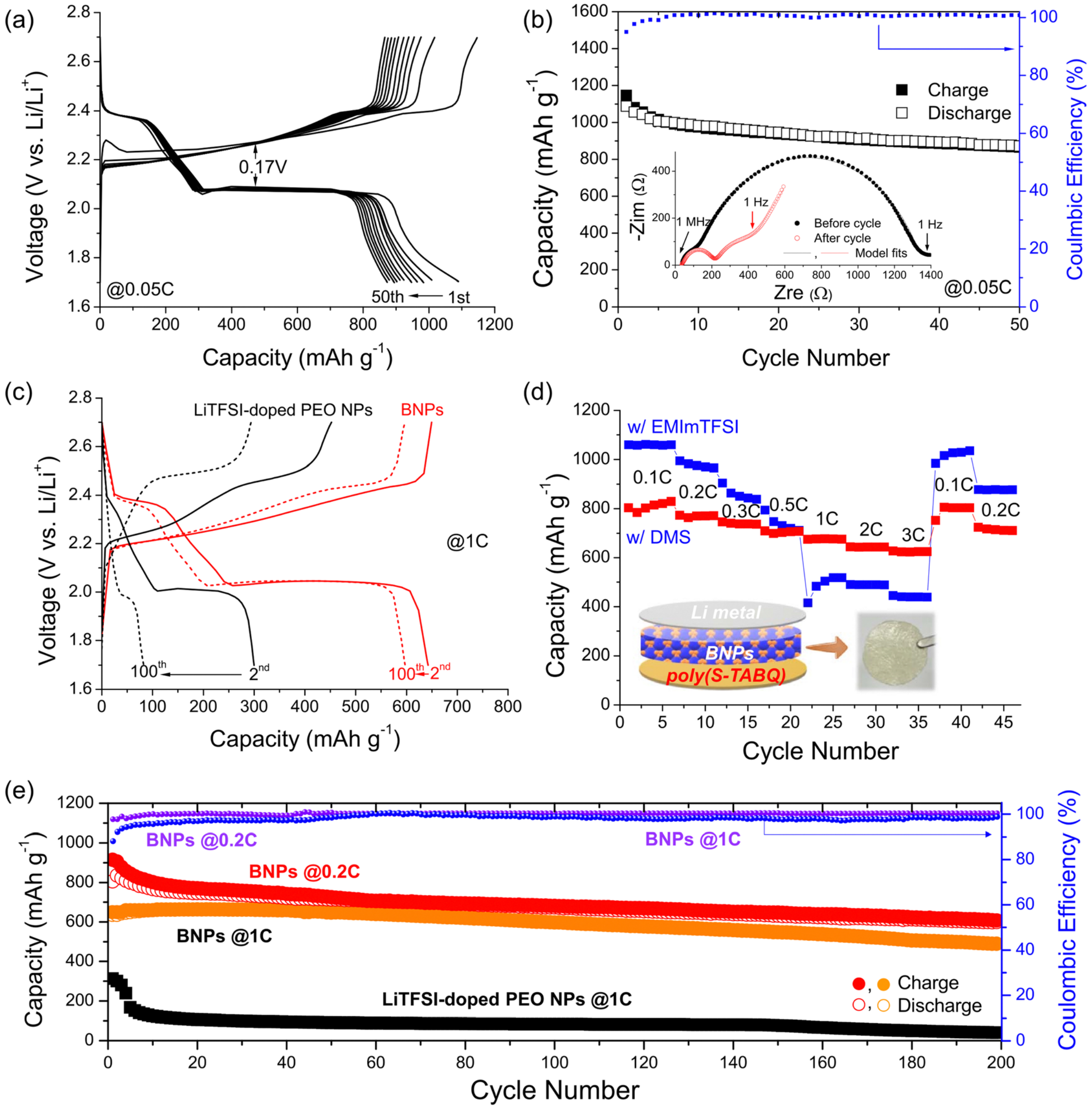

Fig. 4 (a) Galvanostatic charge–discharge voltage profiles, (b) specific capacities and coulombic efficiency of Li/BNPs/poly(S-TABQ) cells, measured at 0.05C and 25 °C. (c) Comparison of galvanostatic charge–discharge voltage profiles for Li/BNPs/poly(S-TABQ) cell at 1C and 25 °C, with Li/LiTFSI-doped PEO NPs/poly(S-TABQ). (d) Rate performance of Li-poly(S-TABQ) cells fabricated with BNPs using different additives, measured at 25 °C. (e) Cycle life of Li-poly(S-TABQ) cells with BNPs at 25 °C, compared to the cells with LiTFSI-doped PEO NPs, over 200 cycles.

electrolyte interphase (SEI) on the electrode surface, which is supported by the Nyquist plots in the inset. The high, stable high CE values indicate that polysulfide shuttle effects in Li–S cells were effectively mitigated by utilizing the BNPs electrolyte, which can be rationalized by two main factors. First, the dissolution of anionic polysulfide intermediates in the gaps between the PEO NPs and PS(LiTFSI) NPs was significantly suppressed. Second, the negatively charged surfaces of the PS(LiTFSI) NPs, which possess a large surface area, induced electrostatic repulsion, further impeding the diffusion of polysulfide species. Additional support for this can be found in Fig. S8 (ESI†), where results from polysulfide diffusion tests are shown.

The performance of Li–S cells heavily relied on the conductivity of BNPs electrolytes. Fig. S9 (ESI†) displays a comparison of galvanostatic charge–discharge voltage profiles for Li/BNPs (AB_6)/S cell and Li/BNPs (AB_3)/S cell. The BNPs with AB_3 had 4.5 times lower conductivity than the AB_6 counterpart (Fig. 3a). This led to an increase in cell polarization from 0.17 to 0.22 V and a decrease in specific capacity from 1090 to 695 mA h g^{-1}.

The galvanostatic discharge–charge voltage profiles of Li–S cells using BNPs and LiTFSI-doped PEO NPs at 1C and 25 °C are compared in Fig. 4c. Initially, the Li cell fabricated with the BNPs delivered a discharge capacity of 621 mA h g^{-1}, which decreased slightly after 100 cycles to 597 mA h g^{-1}, corresponding to a capacity retention of 96%, coupled with a high CE of 100%. In contrast, lithium cells with LiTFSI-doped PEO NPs showed a considerably low initial specific capacity, which rapidly decayed during subsequent charge and discharge processes. The initial discharge capacity was 299 mA h g^{-1}, which was less than half that of BNPs-based Li cells, because of the low ionic conductivity of LiTFSI-doped PEO NPs at 25 °C owing to PEO crystallization. The CE value was extremely poor (150%) owing to the low $t_{\mathrm{Li}}{}^{+}$ of less than 0.3 (Fig. 3d). After 100 cycles, the cell failed to deliver meaningful capacity, exhibiting a very low discharge capacity of 83 mA h g^{-1} with a CE value of 354%, which could be attributed to uncontrollable parasitic reactions at the Li metal surface with depleted TFSI^{-} anions (from LiTFSI salt). These results highlight the importance of designing single-ion polymer electrolytes with BNPs geometries to enhance the Li^{+} transport rates and suppress uncontrolled parasitic reactions at the electrode/electrode interface. The enhanced Li^{+} diffusivity in Li cells using BNPs electrolyte was further validated through cyclic voltammetry (CV) experiments conducted at different scan rates, confirming the excellent redox kinetics of the sulfur cathodes achieved by employing the BNPs electrolyte. (Fig. S10, ESI†)

Fig. 4d presents the discharge capacities of Li/BNPs/poly(S-TABQ) cells at 25 °C, with varying the C-rates. The insets provide a schematic illustration of the Li cells and a digital photograph of the freestanding BNPs membrane. By employing BNPs with DMS, the Li cells demonstrated a remarkable rate capability: 804 (0.1C), 774 (0.2C), 746 (0.3C), 710 (0.5C), 675 (1C), 645 (2C), and 627 mA h g^{-1} (3C). Following high-C-rate tests, the Li cells demonstrated reversible discharge capacities when cycled at 0.1C, which was attributed to the high $t_{\mathrm{Li}}{}^{+}$ value (Fig. 3d). Such behavior was not consistently observed when EMImTFSI was employed as an additive. When BNPs with EMImTFSI was used, the discharge capacities at low C-rates were high as 1060, 974, and 845 mA h g^{-1} at 0.1C, 0.2C, and 0.3C, respectively, owing to the improved ionic conductivity (Fig. 3a). However, the capacity rapidly decreased as the C-rate was further increased, resulting in capacities of 500, 489, 438 mA h g^{-1} at 1C, 2C, and 3C, respectively. This could be attributed to the presence of mobile TFSI^{-} anions from the embedded EMImTFSI. Although the ionic liquid content was low (10 wt%), its localization in the nanoscale gaps of the PEO NPs led to a high local concentration that could not effectively prevent parasitic reactions at the Li metal surfaces.

Moreover, Li/BNPs/poly(S-TABQ) cells with DMS demonstrated an extended cycle life. Fig. 4e presents the representative discharge capacities and CE values obtained at 0.2C and 1C. At 0.2C, an initial discharge capacity of 806 mA h g^{-1} was achieved, which decreased to 608 mA h g^{-1} after 200 cycles. Similarly, at 1C, the initial discharge capacity was 650 mA h g^{-1}, with a final capacity of 490 mA h g^{-1} after 200 cycles. At both C-rates, a capacity retention of 75% was attained and the CE values remained consistently high, exceeding 99% after 200 cycles. It should be noted here that CE values at 1C reached 100% in the first 5 cycles, whereas at 0.2C, it started at 95% after 5 cycles and increased with successive cycles. The lower CE values at lower C rates can be attributed to a small but irreversible loss of polysulfide trapped in BNPs electrolytes during discharge. Slower polysulfide diffusion through BNPs compared to polysulfide formation contributed to this, particularly noticeable at low C rates.

In Fig. S11 (ESI†), we presented additional performance data for Li–S cells with conventional elemental sulfur-carbon cathodes. Consistently, the results demonstrate that the utilization of BNPs electrolytes significantly improved capacity and rate performance of Li–S cells compared to the control cells using LiTFSI-doped PEO NPs or liquid electrolytes. It is worth mentioning that cells fabricated with PEO/PS(LiTFSI) blends were unable to operate at room temperature.

The utilization of single-ion-conducting polymer binders in Li–S batteries has recently been investigated.[42–44] However, successful applications of single-ion polymers as solid-state electrolytes for Li–S batteries remain scarce. Previous studies mainly focused on using single-ion polymers as functional separators[43] or binders[44] for sulfur cathodes. Alternatively, researchers have attempted to prepare membranes by blending single-ion polymers with conventional nonionic polymers,[45] such as poly(vinylidene fluoride-*co*-hexafluoropropylene). Unfortunately, these membranes had to be soaked in liquid electrolytes to operate Li–S batteries. This study represents the first demonstration of utilizing an all-solid-state single-ion polymer with exceptional mechanical and electrochemical stability over wide temperature and voltage ranges in Li–S batteries. Furthermore, we have addressed contact-related issues in rigid components by incorporating non-flammable additives with high dielectric constants. These findings hold great significance, particularly for the utilization of single-ion polymer-ceramic composites as solid-state electrolytes in emerging battery technologies.

Conclusions

We developed all-solid-state Li–S batteries with significantly improved electrochemical stability, rate performance, and cycle life. These advancements were achieved through the strategic design of single-ion electrolytes utilizing the co-assembly of two types of core–shell NPs with different sizes and in different number ratios. By combining Li^{+}-donating PS(LiTFSI) NPs with Li^{+}-transporting PEO NPs, we achieved a room-temperature ionic conductivity of 10^{-4} S cm^{-1}, a lithium transference number of 0.94, and a mechanical strength of $\sim$0.1 GPa over a wide temperature range. The resulting Li–S batteries demonstrated outstanding performance, with a discharge capacity exceeding 1008 mA h g^{-1} and high CE ($>$99%). They also exhibited excellent rate performance, with a discharge capacity of 627 mA h g^{-1} at 3C. Moreover, the batteries demonstrated a stable cycle life, retaining a discharge capacity of $>$600 mA h g^{-1} even after 200 cycles at 0.2C. Our findings will pave the way for the safe operation of future high-energy-density lithium batteries utilizing solid-state hybrid electrolytes.

Author contributions

Moon Jeong Park conceived the idea and designed the project. Boram Kim carried out the experiments and analyzed data. Moon Jeong Park and Boram Kim wrote the manuscript.

Conflicts of interest

There are no conflicts to declare.

Acknowledgements

This work is financially supported by the National Research Foundation of Korea (NRF) grant funded by the Korea government (No. NRF-2022R1A2C3004667) (No. NRF-2017R1A5A1015365). (NRF-2018M3D1A1058624). Prof. Park also acknowledge financial support from Korea Toray Science Foundation.

References

1 Y. Kato, S. Hori, T. Saito, K. Suzuki, M. Hirayama, A. Mitsui, M. Yonemura, H. Iba and R. Kanno, *Nat. Energy*, 2016, **1**, 16030.
2 R. Bouchet, S. Maria, R. Meziane, A. Aboulaich, L. Lienafa, J.-P. Bonnet, T. N. T. Phan, D. Bertin, D. Gigmes, D. Devaux, R. Denoyel and M. Armand, *Nat. Mater.*, 2013, **12**, 452.
3 X. Lin, S. Xu, Y. Tong, X. Liu, Z. Liu, P. Li, R. Liu, X. Feng, L. Shi and Y. Ma, *Mater. Horiz.*, 2023, **10**, 859.
4 R. Chen, W. Qu, X. Guo, L. Li and F. Wu, *Mater. Horiz.*, 2016, **3**, 487.
5 Z.-J. Zheng, H. Ye and Z.-P. Guo, *Adv. Sci.*, 2020, **7**, 2002212.
6 S. Rajendran, Z. Tang, A. George, A. Cannon, C. Neumann, A. Sawas, E. Ryan, A. Turchanin and L. M. R. Arava, *Adv. Energy Mater.*, 2021, **11**, 2100666.
7 X. Xu, K. S. Hui, K. N. Hui, H. Wang and J. Liu, *Mater. Horiz.*, 2020, **7**, 1246.
8 T. Famprikis, P. Canepa, J. A. Dawson, M. S. Islam and C. Masquelier, *Nat. Mater.*, 2019, **18**, 1278.
9 X. Feng, H. Fang, N. Wu, P. Liu, P. Jena, J. Nanda and D. Mitlin, *Joule*, 2022, **6**, 543.
10 A. Banerjee, X. Wang, C. Fang, E. A. Wu and Y. S. Meng, *Chem. Rev.*, 2020, **120**, 6878.
11 Z. Zhang, Y. Shao, B. Lotsch, Y.-S. Hu, H. Li, J. Janek, L. F. Nazar, C.-W. Nan, J. Maier, M. Armand and L. Chen, *Energy Environ. Sci.*, 2018, **11**, 1945.
12 Z. Zhang, Y. Shao, B. Lotsch, Y.-S. Hu, H. Li, J. Janek, L. F. Nazar, C.-W. Nan, J. Maier, M. Armand and L. Chen, *Energy Environ. Sci.*, 2018, **11**, 1945.
13 T. W. Kim, K. H. Park, Y. E. Choi, J. Y. Lee and Y. S. Jung, *J. Mater. Chem. A*, 2018, **6**, 840.
14 S. Xin, Y. You, S. Wang, H.-C. Gao, Y.-X. Yin and Y.-G. Guo, *ACS Energy Lett.*, 2017, **2**, 1385.
15 Y. Zhao, L. Wang, Y. Zhou, Z. Liang, N. Tavajohi, B. Li and T. Li, *Adv. Sci.*, 2021, **8**, 2003675.
16 D. G. Mackanic, X. Yan, Q. Zhang, N. Matsuhisa, Z. Yu, Y. Jiang, T. Manika, J. Lopez, H. Yan, K. Liu, X. Chen, Y. Cui and Z. Bao, *Nat. Commun.*, 2019, **10**, 5384.
17 H. Y. Jung, P. Mandal, G. Jo, O. Kim, M. Kim, K. Kwak and M. J. Park, *Macromolecules*, 2017, **50**, 3224.
18 M. Singh, O. Odusanya, G. M. Wilmes, H. B. Eitouni, E. D. Gomez, A. J. Patel, V. L. Chen, M. J. Park, P. Fragouli, H. Iatrou, N. Hadjichristidis, D. Cookson and N. P. Balsara, *Macromolecules*, 2007, **40**, 4578.
19 B. K. Wheatle, J. R. Keith, S. Mogurampelly, N. A. Lynd and V. Ganesan, *ACS Macro Lett.*, 2017, **6**, 1362.
20 L. Shi, C. Zhang, Y. Du, H. Zhu, Q. Zhang and S. Zhu, *Adv. Funct. Mater.*, 2021, **31**, 2007863.
21 M. J. Park, *Mol. Syst. Des. Eng.*, 2019, **4**, 239.
22 D. Lee, H. Y. Jung and M. J. Park, *ACS Macro Lett.*, 2018, **7**, 1046.
23 J. Kim, K.-J. Jeong, K. Kim, C. Y. Son and M. J. Park, *Macromolecules*, 2022, **55**, 2028.
24 S. Kadulkar, Z. W. Brotherton, A. L. Lynch, G. Pohlman, Z. Zhang, R. Torres, A. Manthiram, N. A. Lynd, T. M. Truskett and V. Ganesan, *Macromolecules*, 2023, **56**, 2790.
25 S. Liu, W. Liu, D. Ba, Y. Zhao, Y. Ye, Y. Li and J. Liu, *Adv. Mater.*, 2023, **35**, 2110423.
26 Z. Zhu, M. Hong, D. Guo, J. Shi, Z. Tao and J. Chen, *J. Am. Chem. Soc.*, 2014, **136**, 16461.
27 F. Croce, G. B. Appetecchi, L. Persi and B. Scrosati, *Nature*, 1998, **394**, 456.
28 X. Fu, D. Yu, J. Zhou, S. Li, X. Gao, Y. Han, P. Qi, X. Feng and B. Wang, *CrystEngComm*, 2016, **18**, 4236.
29 D. Lin, W. Liu, Y. Liu, H. R. Lee, P.-C. Hsu, K. Liu and Y. Cui, *Nano Lett.*, 2016, **16**, 459.
30 B. W. Zewde, S. Admassie, J. Zimmermann, C. S. Isfort, B. Scrosati and J. Hassoun, *ChemSusChem*, 2013, **6**, 1400.
31 S. Choudhury, S. Stalin, Y. Deng and L. A. Archer, *Chem. Mater.*, 2018, **30**, 5996.
32 J. L. Schaefer, D. A. Yang and L. A. Archer, *Chem. Mater.*, 2013, **25**, 834.
33 H. Zhang, C. Li, M. Piszcz, E. Coya, T. Rojo, L. M. Rodriguez-Martinez, M. Armand and Z. Zhou, *Chem. Soc. Rev.*, 2017, **46**, 797.
34 E. Glynos, L. Papoutsakis, W. Pan, E. P. Giannelis, A. D. Nega, E. Mygiakis, G. Sakellariou and S. H. Anastasiadis, *Macromolecules*, 2017, **50**, 4699.
35 M. Li, J. E. Frerichs, M. Kolek, W. Sun, D. Zhou, C. J. Huang, B. J. Hwang, M. R. Hansen, M. Winter and P. Bieker, *Adv. Funct. Mater.*, 2020, **30**, 1910123.
36 J. Zhu, Z. Zhang, S. Zhao, A. S. Westover, I. Belharouak and P.-F. Cao, *Adv. Energy Mater.*, 2021, **11**, 2003836.
37 B. Kim, H. Kang, K. Kim, R.-Y. Wang and M. J. Park, *ChemSusChem*, 2020, **13**, 2271.
38 Y.-G. Lee, J.-H. Park, C. Oh, S.-G. Oh and Y. C. Kim, *Langmuir*, 2007, **23**, 10875.
39 J. Evans, C. A. Vincent and P. G. Bruce, *Polymer*, 1987, **28**, 2324.
40 J.-N. Chazalviel, *Phys. Rev. A: At., Mol., Opt. Phys.*, 1990, **42**, 7355.
41 H. Kang, H. Kim and M. J. Park, *Adv. Energy Mater.*, 2018, **8**, 1802423.
42 Z. Li, W. Lu, N. Zhang, Q. Pan, Y. Chen, G. Xu, D. Zeng, Y. Zhang, W. Cai, M. Yang, Z. Yang, Y. Sun, H. Ke and H. Cheng, *J. Mater. Chem. A*, 2018, **6**, 14330.
43 B. Huang, H. Hua, P. Lai, X. Shen, R. Li, Z. He, P. Zhang and J. Zhao, *ChemElectroChem*, 2022, **9**, e20220041.
44 P. T. Dirlam, R. S. Glass, K. Char and J. Pyun, *J. Polym. Sci. Part A: Polym. Chem.*, 2017, **55**, 1635.
45 H.-P. Liang, M. Zarrabeitia, Z. Chen, S. Jovanovic, S. Merz, J. Granwehr, S. Passerini and D. Bresser, *Adv. Energy Mater.*, 2022, **12**, 2200013.